

# Quantifying Atmospheric Impacts on Space Optical Imaging and Communications

**Randall J. Alliss and Billy D. Felton**

*Northrop Grumman Information Systems  
3975 Virginia Mallory Drive  
Chantilly, VA 20151*

## ABSTRACT

Clouds and optical turbulence are key drivers in the performance of optical imaging and communication systems. Clouds are composed of liquid water and/or ice crystals and depending on the physical thickness can produce atmospheric fades easily exceeding 10 dB. In these more common cases, impacts on optical imaging and communication systems may be severe. On the other hand, there are times when cloud fades may be as low as 1 or 2 dB as a result of thin, ice crystal based cirrus clouds. In these cases, the impacts on imaging and communication collectors may be limited. Atmospheric optical turbulence acts to distort light in the atmosphere, degrading imagery from telescopes. The quality of service of a free space optical communications link may also be impacted. Some of the degradation due to turbulence can be corrected by adaptive optics. However, the severity of optical turbulence, and thus the amount of correction required, is largely dependent upon distributions of turbulence at the location of interest. Large variations in the Fried Coherence Length ( $r_0$ ) are common as a function of time of day and by location and can range from just a few centimeters to tens of centimeters.

The ability to characterize the distribution and frequency of clouds and optical turbulence are critical in order to understand and predict atmospheric impacts. A state-of-the-art cloud detection system has been developed, validated and applied to produce high resolution climatologies in order to investigate these impacts. The cloud detection system uses global in coverage, geostationary, multi-spectral satellite imagery at horizontal resolutions up to one kilometer and temporal resolutions up to fifteen minutes. Multi-spectral imagery from the visible wavelengths (0.6  $\mu\text{m}$ ) through the longwave infrared (15  $\mu\text{m}$ ) are used to produce individual cloud tests which are combined to produce a composite cloud analysis. The basis for the detection algorithm relies on accurate modeling of the clear sky background (CSB). The CSB represents a recent depiction (one month weighted average) of what the scene looks like, radiometrically, in the absence of clouds so that it can be compared with imagery at the requested analysis time. If the actual imagery compared to the CSB differs by more than a specified threshold then clouds are indicated. Cloud properties such as cloud top heights and bases and optical depths are subsequently derived. The result represents a high spatial and temporal resolution climatology that can be used to derive accurate Cloud Free Line of Sight (CFLOS) statistics in order to quantify atmospheric effects on optical imaging and communication systems. For example, clouds over the State of Hawaii are quite variable in frequency ranging from less than 15% in some of the sheltered coastal waters and local summits to greater than 70% on the mauka (windward) sides of the islands. Vertical optical depths from the summit can range from 0.5dB to greater than 50dB.

Optical turbulence is characterized by the refractive index structure function  $C_n^2$ , which in turn is used to calculate atmospheric seeing parameters. While attempts have been made to characterize  $C_n^2$  using empirical models, it can be calculated more directly from Numerical Weather Prediction (NWP) simulations using pressure, temperature, thermal stability, vertical wind shear, turbulent Prandtl number, and turbulence kinetic energy (TKE). A modified version of the Weather Research and Forecast (WRF) model is used to generate  $C_n^2$  throughout the atmospheric column, allowing for ground-to-space seeing estimates of  $r_0$ . Simulations are performed using the Maui High Performance Computing Centers (MHPCC) Mana cluster.

Detailed results from both the clouds and turbulence simulations will be shown at the conference with specific applications to space imaging and communication systems.

**Keywords:** cloud free line of sight, optical turbulence, optical communications, WRF, GOES

## 1. INTRODUCTION

Optical turbulence (OT) is important to astronomers and designers of free-space optical communications systems because of the impact it has on the quality of the optical wavefront. Generated by small-scale variations in the temperature and moisture of air, optical turbulence produces fluctuations in the atmospheric index of refraction. As electromagnetic waves travel through the atmosphere, these inhomogeneities in the refractive index produce changes in the phase and intensity of electromagnetic waves and distort the original wavefront. The intensity of the turbulent fluctuations of the atmospheric refractive index is described by the refractive index structure function,  $C_n^2$ .

Some of the degradation due to turbulence can be corrected by adaptive optics (AO). However, the severity of optical turbulence, and thus the amount of correction required, can vary significantly for different locations. Therefore, it is vital to understand the climatology of optical turbulence at such locations. This can impact decisions on site selection, AO system design, and observatory scheduling. In many cases, it is impractical and expensive to set up and operate instrumentation to characterize the climatology of optical turbulence, so simulations become a more economical and convenient alternative.

Numerical simulations offer many advantages over direct measurements. They provide a three-dimensional (3D) description of  $C_n^2$  over regions of interest. Simulations can be performed for any region on Earth, making them a valuable asset for assessing potential new sites. Additionally, with High Performance Computing (HPC) platforms becoming much more affordable and accessible, long-term climatologies sampling multiple years, seasons, and times of day can be produced in a relatively short period of time. Finally, numerical simulations can provide forecasts of optical turbulence that can be used for scheduling purposes. The reliability of these types of simulations for describing the climatology of optical turbulence has recently been shown to be quite good.

Our approach to simulating optical turbulence employs a model used to predict tropospheric weather. The meteorological community refers to such models as Numerical Weather Prediction (NWP) models, and uses them to make weather forecasts on a daily basis. However, for this application, we have modified the model to make simulations of  $C_n^2$ . In this paper we describe how NWP is leveraged to simulate optical turbulence, and present various results along with intercomparisons to direct observations of seeing parameters.

## 2. TECHNICAL APPROACH

The results of this investigation were computed using version 3.0 of the Weather Research & Forecasting (WRF) model (Skamarock, 2008), developed jointly between the National Center for Atmospheric Research (NCAR) and the National Oceanic and Atmospheric Administration (NOAA). WRF is a mesoscale NWP model developed for the prediction of weather, and is routinely used by the National Weather Service and other forecasting services. The model is based on the Navier-Stokes equations which are solved numerically on a three dimensional grid. The model simulates four basic atmospheric properties – wind, pressure, temperature, and atmospheric water vapor. All other variables are derived from these four parameters.

The WRF model is being used to develop climatologies of optical turbulence for several regions in the United States. This study focuses on simulations near Albuquerque, NM. The following sections describe the model setup, modifications to the code, and derivation of optical turbulence parameters.

### 2.1 Model Setup

WRF is used to simulate daily meteorological conditions for several regions in the United States for the period 2006–2007. In each case the model is configured at 1-km horizontal resolution with dimensions 67×63. The number of vertical grid points varies from 135 to 140, with the sigma levels set to approximate 50-m resolution below 2 km above ground level (AGL), 125 m for 2–12 km AGL, and 500 m up to the model top (50 millibars). Simulations are initialized at 1200 UTC directly from the 12-km North American Mesoscale (NAM) analysis produced by the National Weather Service. Lateral boundary conditions are provided out to 27 hours by three-hourly NAM forecasts. This allows for filtering out model “spin-up” by excluding the first three simulation hours, while still capturing the full 24-hour diurnal cycle. Selected physics and diffusion options are summarized in Table 1.

Table 1 Physics and diffusion settings used in WRF model for this study

<i>Parameter</i>	<i>Value</i>
Time Integration	RK3
Time Step	2 seconds
Horizontal/Vertical Advection	Fifth/Third order
Explicit Diffusion	Physical space 2D deformation, no sixth order
Boundary Layer Physics	Modified Mellor, Yamada, Janjic (MYJ)
Surface Layer	Janjic Eta
Land Surface	Noah
Shortwave/Longwave Radiation	Dudhia/RRTM
Microphysics	WSM6
Cumulus Parameterization	None

## 2.2 Model Modifications

Initial tests revealed that the minimum turbulence kinetic energy (*TKE*) permitted in the Mellor-Yamada-Janjic (MYJ) scheme within WRF had to be modified. The default setting gives *TKE* values  $\geq 0.1 \text{ m}^2\text{s}^{-2}$ , resulting in unrealistically large values of  $C_n^2$  in the free atmosphere. Following Gerrity et al. 1994, the minimum *TKE* limit was changed to  $10^{-5} \text{ m}^2\text{s}^{-2}$ . A second modification was made to address NWP under-prediction of turbulence in the free atmosphere. Walters and Miller, 1999 found that the Mellor and Yamada 2.5 order turbulence parameterization does not produce sufficient *TKE* (by several orders of magnitude) in the free atmosphere where thermally stable conditions persist. Walters and Miller proposed a change to the way the eddy diffusivities of heat and momentum ( $K_H$  and  $K_M$ , respectively) are calculated. The MYJ prognostic equation for *TKE* ( $e$ ) can be written:

$$\frac{\partial e}{\partial t} = \underset{\text{I}}{K_M \left( \frac{\partial U}{\partial z} \right)^2} - \underset{\text{II}}{K_H \frac{g}{\theta} \left( \frac{\partial \theta}{\partial z} \right)} - \underset{\text{III}}{\frac{(2e)^{3/2}}{11.88l}} - \underset{\text{IV}}{U_i \left( \frac{\partial e}{\partial x_i} \right)} + \underset{\text{V}}{\frac{\partial}{\partial z} \left[ 0.2l\sqrt{2e} \frac{\partial e}{\partial z} \right]} \quad (1)$$

where  $\theta$  is the potential temperature,  $l$  is the mixing length,  $e$  is the *TKE*, and

- Term **I** is a mechanical or Shear production/loss term. Large positive values of wind shear (vertical gradient of horizontal wind speed/direction) tend to produce turbulence;
- Term **II** is the Bouyancy production/consumption term. Turbulence is produced when  $\partial\theta/\partial z$  is negative (less dense air under more dense air);
- Term **III** is viscous dissipation of turbulence;
- Term **IV** is advection of turbulence;
- Term **V** is diffusion of turbulence.

In a statically stable environment (i.e.,  $\partial\theta/\partial z > 0$ ), the bouyancy term (II) acts to suppress turbulence, so the magnitude of the shear term (I) dictates whether turbulence can exist. The ratio of these two terms (the Richardson number,  $Ri$ ) indicates the likelihood of the presence of turbulence. The gradient Richardson number is given by:

$$Ri = \frac{g}{\theta} \frac{\frac{\partial \theta}{\partial z}}{\left[ \left( \frac{\partial u}{\partial z} \right)^2 + \left( \frac{\partial v}{\partial z} \right)^2 \right]} \quad (2)$$

Laminar flow becomes turbulent when  $Ri$  is smaller than the critical Richardson number,  $R_c$ . Turbulent flow becomes laminar when  $Ri$  is greater than  $R_T$ . Research has shown that  $R_c = 0.25$  and  $R_T = 1.0$ . Thus, turbulence may or may not exist in the region where  $0.25 < Ri < 1.0$ , dependent upon whether the previous state of the atmosphere was turbulent or laminar.

In a literature review, Walters and Miller, 1999 found that the gradient Richardson number is a poor indicator of turbulence under thermally stable conditions. They suggested a more realistic parameterization of  $K_H$  and  $K_M$  that takes into account the possibility that turbulence exists where  $Ri > R_c$ . In the original MYJ scheme,  $K_H$  and  $K_M$  are given by:

$$K_H = lqS_H \quad (3)$$

$$K_M = lqS_M \quad (4)$$

where  $l$  is the mixing length,  $q = \sqrt{2TKE}$ , and  $S_H$  and  $S_M$  are functions of  $TKE$ , mixing length, buoyancy, and vertical wind shear (Skamarock, 2008). In the version of WRF used for this work, these relations are unchanged for neutral and unstable conditions. However, based upon Walters and Miller, when the gradient Richardson number ( $Ri$ )  $> 0.01$ ,  $K_M$  is adjusted within WRF such that:

$$\frac{K_H}{K_M} = \begin{cases} \frac{1}{7Ri} & \text{for } Ri \geq 1, \\ \frac{1}{6.873Ri + \frac{1}{1.6873Ri}} & 0.01 < Ri \leq 1. \end{cases} \quad (5)$$

This equation for  $K_H/K_M$  was first proposed by Kondo et al. 1978. The Kondo equation decreases  $K_H/K_M$  with increasing  $Ri$  (Figure 1), effectively increasing  $TKE$  production by vertical wind shear (Term I in Equation 1) by reducing the consumption of turbulence by buoyancy forces (Term II in Equation 1). Walters and Miller found this necessary to generate free atmosphere turbulence associated with jet streaks, and this change is in effect in all WRF simulations for this work.

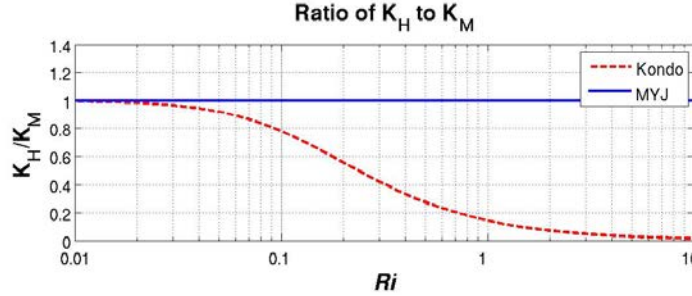


Figure 1 Kondo parameterization of  $K_H$  and  $K_M$  as a function of Richardson number.

### 2.3 Derivation of Atmospheric Seeing

Traditionally, the atmospheric optical turbulence of astronomical observatories, and more recently potential optical communications ground stations, has been quantified in terms of astronomical seeing. The Fried parameter ( $r_0$ ), or transverse coherence length, is one such seeing parameter, and is calculated for a plane wave by integrating  $C_n^2$  along a path by

$$r_0 = \left[ 0.423 \left( \frac{2\pi}{\lambda} \right)^2 \int_0^{\infty} C_n^2(z) dz \right]^{-3/5} \quad (6)$$

where  $\lambda$  is the optical wavelength. Fried introduced  $r_0$  to measure the magnitude of the phase distortion of an optical wavefront by turbulence (Fried, 1965). Smaller values of  $r_0$  indicate more severe turbulence, and increasingly degraded atmospheric seeing conditions. Knowledge of the statistics of  $r_0$  for a given location is important to adaptive optics

system designers because  $r_0$  determines the spacing of the actuators required to compensate for the wavefront distortions produced by the turbulence.

Despite running WRF at very high resolution, turbulence still occurs on scales smaller than the model can resolve explicitly. Therefore, the turbulence must be parameterized based on the resolvable meteorological parameters calculated by WRF. The temperature, pressure, and winds that are calculated explicitly by WRF are combined with the *TKE* parameterized by WRF to generate a three-dimensional characterization of  $C_n^2$  as described in Equations 7–14. From this, the point-to-point estimates of  $r_0$  required by system designers can be calculated using Equation 6.

When turbulence is locally homogeneous and isotropic,  $C_n^2$  is related to changes in the refractive index  $\delta n$  over distance,  $r$ :

$$\overline{(\delta n)^2} = C_n^2 r^{2/3} \quad (7)$$

where the overbar indicates an ensemble average, and  $r$  lies within the inertial subrange of turbulence (Tatarski, 1971). Larger values of  $C_n^2$  correspond to increasing changes in the refractive index. Tatarski derived an alternative expression for the structure-function parameter applicable for optical wavelengths:

$$C_n^2 = \left( \frac{79 \times 10^{-8} P}{T^2} \right)^2 C_T^2 \quad (8)$$

where  $P$  is atmospheric pressure (Pa),  $T$  is air temperature (K), and  $C_T^2$  is the structure function parameter for temperature.  $C_T^2$  is calculated by:

$$C_T^2 = a^2 \left( \frac{K_H}{K_M} \right) L_o^{4/3} \left( \frac{\partial \theta}{\partial z} \right)^2 \quad (9)$$

where  $a^2$  is an empirical constant,  $L_o$  is the outer length scale of turbulence (i.e., the upper bound of the inertial subrange),  $K_H$  and  $K_M$  are the eddy diffusivities of heat and momentum, and  $\partial \theta / \partial z$  is the vertical gradient of potential temperature. Following Walters and Miller, 1999,  $a^2$  is set to 2.8.  $L_o$  is calculated in thermally stable conditions using an approximation from Deardorff (1980):

$$L_o = 0.76 \frac{\sqrt{TKE}}{N} \quad (10)$$

where  $N$  is the Brunt-Väisälä frequency given by:

$$N = \sqrt{\frac{g}{\theta} \frac{\partial \theta}{\partial z}} \quad (11)$$

In thermally unstable conditions,  $L_o$  is related to the depth of the unstable layer, similar to Bougeault and Lacarrere 1989 and Masciadri et al.2001;

$$L_o = (L_{up} J_{down})^{1/2} \quad (12)$$

where

$$\int_z^{z+L_{up}} \frac{g}{\theta} (\theta(z) - \theta(z')) dz' = e(z) \quad (13)$$

and

$$\int_{z-L_{down}}^z \frac{g}{\theta} (\theta(z') - \theta(z)) dz' = e(z) \quad (14)$$

This algorithm for calculating  $C_n^2$  within WRF is the basis for the results that follow.

### 3. RESULTS

Three-dimensional turbulence simulations were made over the state of New Mexico once per day for 23 months during 2007-2008. Figure 2 summarizes a year of simulations over ABQ in a time/height plot of  $C_n^2$  (i.e., Hovmoller diagram). Data are plotted every hour during the year for each of the 137 vertical levels. The data show how  $C_n^2$  varies with time. Red shaded ( $\sim 10^{-14}$ ) areas denote higher turbulence, and darker blue shades ( $\sim 10^{-18}$ ) indicate where turbulence is more benign. The figure indicates that the highest values of  $C_n^2$  are found in the boundary layer (lowest 1.5 km). This is to be expected because solar insolation at the ground produces large heat fluxes, resulting in greater turbulence. Values can be as high as  $10^{-13}$  on a hot summer afternoon when solar heating of the desert produces very large heat fluxes. Although the diurnal variation in  $C_n^2$  is not visible in this figure, a large variation does exist (see later figures). Above the boundary layer, the  $C_n^2$  profile becomes smaller until the jet stream level is reached. The height of the jet stream can vary between 8 and 12 km depending on the time of year. Generally  $C_n^2$  is larger during the winter months at these altitudes because of increased wind shear associated with the jet stream, and smaller during the summer months as the jet weakens and retreats poleward.

The  $r_0$  was derived from  $C_n^2$  (Equation 6) profiles by integrating  $C_n^2$  vertically for each model time step. The WRF-derived values of  $r_0$  were compared to *in situ* measurements from a Differential Image Motion Monitor (DIMM) instrument located near Albuquerque. Figure 3(a) shows the hourly mean, 5% and 95% values of  $r_0$  for the WRF-derived simulations (blue) as well as the DIMM measurements (red). Values of  $r_0$  are shown referenced to 1550 nm because this is a common wavelength for free-space optical communications chosen to minimize water vapor attenuation. Both datasets exhibit similar diurnal cycles with  $r_0$  dropping rapidly after sunrise, reaching a minimum near local noon, and rising back toward its larger nighttime range in the late afternoon. An evening neutral event is also evident in both datasets, with the WRF event somewhat more pronounced. The neutral event, long observed in OT measurements, occurs when the solar insolation decreases near sunset, causing the temperature lapse rate in the planetary boundary layer to be neutrally stable (adiabatic). The overlap in the distributions between the simulations and observations is remarkable. However, in general, the WRF model does not simulate the very smallest values of  $r_0$  in the daytime. This is not surprising given the differences in resolution between the model and the DIMM instrument. WRF is run with a horizontal resolution of one kilometer, whereas the instrument is taking measurements in the line-of-sight of a star. Therefore, it is expected the WRF model will only characterize the mean turbulence over that 1-km<sup>2</sup> area, while the line-of-sight of the DIMM intermittently samples the intense  $C_n^2$  within turbulent plumes as well as more benign areas between plumes.

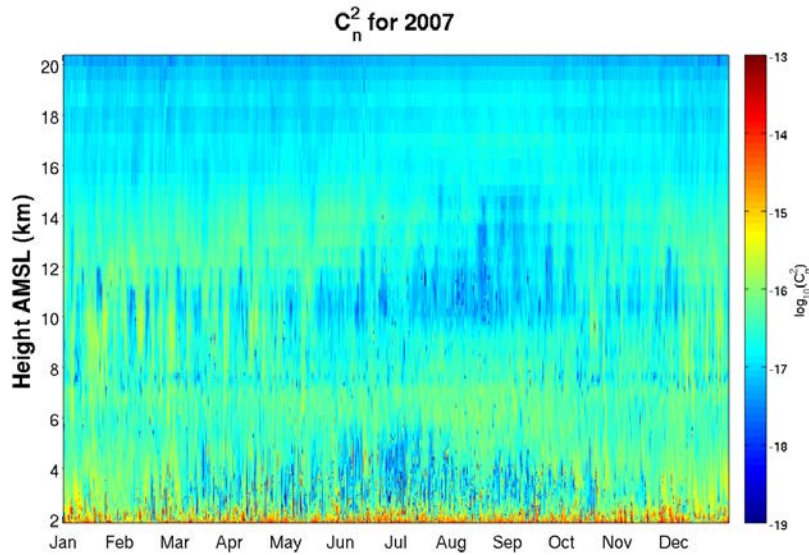


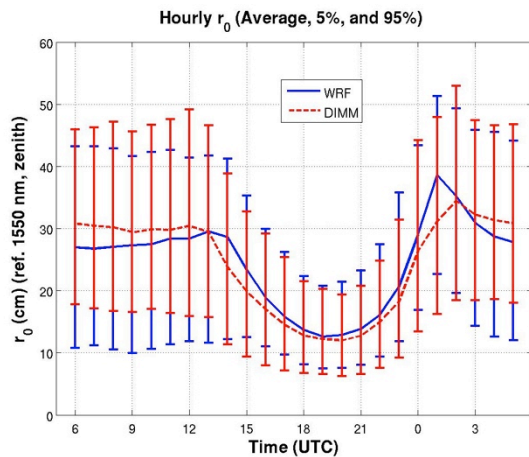
Figure 2  $C_n^2$  as a function of time and height over Albuquerque, NM, during 2007

The cumulative distributions of both datasets for all times, daytime, and nighttime are plotted in Figure 3. Only those simulations of  $r_0$  that had a cloud-free line of sight (CFLOS) are included in this analysis. This is done because the

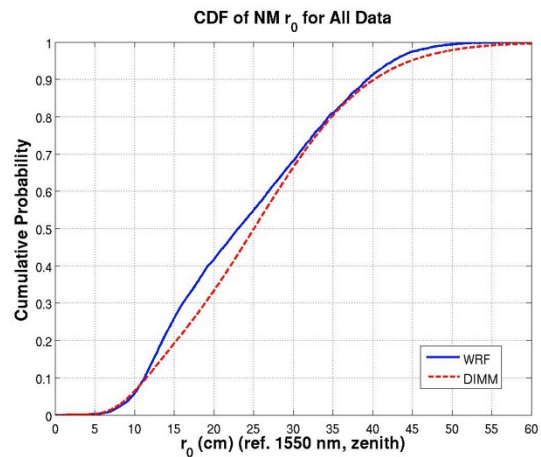
DIMM only makes measurements during CFLOS conditions. The shapes of the distributions are very similar. The median WRF-derived values of  $r_0$  are about 1.1 cm too large in the daytime hours and about 1.4 cm too small at night. Table 2 shows the median  $r_0$  values for the WRF simulations and the DIMM measurements along with their percentage differences for day, night, and all times. The differences are small, ranging from 4.8 – 8.8%.

Table 2 Comparison of Median  $r_0$  from independent WRF simulations to DIMM measurements for Albuquerque domain. Values of  $r_0$  are referenced to 1550 nm.

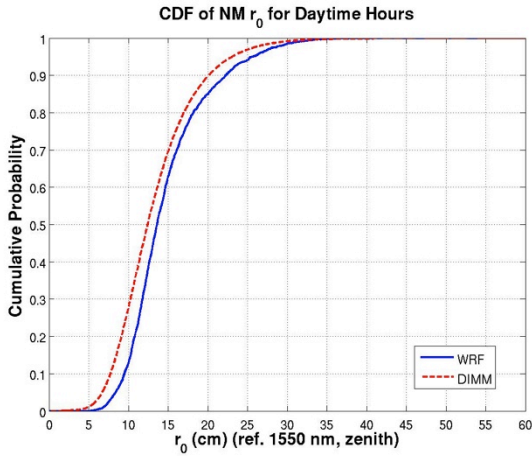
Time of Day	WRF Median $r_0$ (cm)	DIMM Median $r_0$ (cm)	Difference (%)
Day	13.6	12.5	-8.8
Night	27.9	29.3	4.8
All	23.1	25.1	8.0



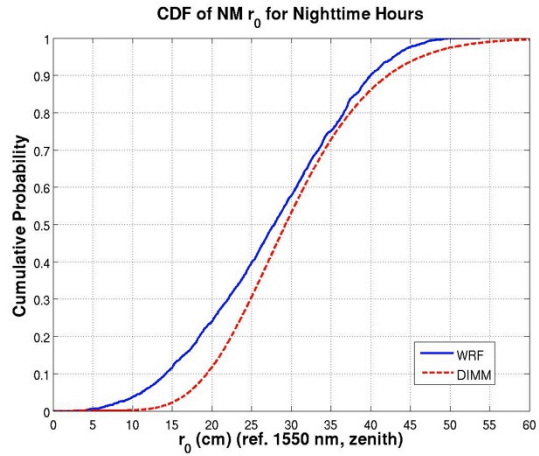
(a)



(b)



(c)



(d)

Figure 3 Hourly mean, 5% and 95% values of  $r_0$  (a) and cumulative distributions of WRF-derived (solid blue) and DIMM  $r_0$  measurements (dashed red) for NM domain. Cumulative distributions are shown for all data (b) and for daytime (c) and nighttime (d) data.

Although WRF is unable to simulate the lowest  $r_0$  during the daytime, it produces smaller values of  $r_0$  than the DIMM measures at night. This is particularly true during the spring and fall months. Upon further investigation, the WRF model is doing an excellent job in simulating the canyon winds that are typical at night in this area. They are most pronounced during the spring and fall months under clear skies with high pressure centered to the northeast of Albuquerque. This condition sets up an easterly wind that is accelerated through the Sandia and Manzano mountain passes underneath a strong temperature inversion. Winds during these events can easily exceed  $20 \text{ ms}^{-1}$  and produce intense low-level turbulence due to strong wind shear. These events are not represented in the DIMM measurement data because the dome in which the DIMM was located was closed to prevent physical damage to the instruments when the wind exceeded  $10 \text{ ms}^{-1}$ . Therefore, the observational climatology of  $r_0$  at this location may be affected at nighttime due to lack of observations. Indeed, there are many fewer observations between 0600 and 1200 UTC in this dataset. When simulations of  $r_0$  during canyon events are eliminated from the analysis, the comparison between WRF and the DIMM improves as shown in Figure 4.

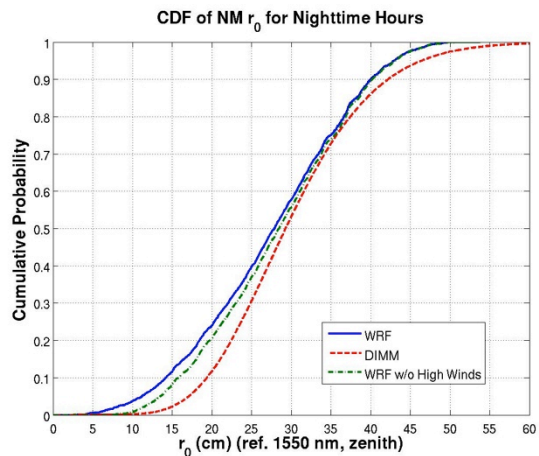
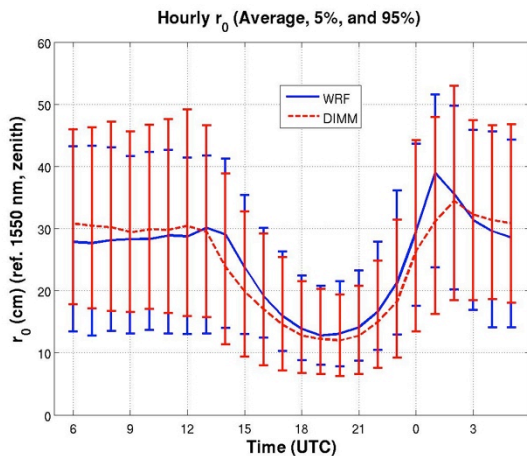


Figure 4 Hourly mean, 5% and 95% values of  $r_0$  (left) and cumulative distributions of WRF-derived (solid blue) and DIMM  $r_0$  measurements (dashed red) for NM domain (right). The dashed green line shows the CDF of  $r_0$  when cases of strong surface winds are removed.

Although the DIMM and other similar instruments are useful in collecting observations for a particular location, it is difficult to collect in many locations simultaneously. The infrastructure to maintain these instruments is large and expensive. However, HPC makes it very convenient and affordable to simulate turbulence over many areas simultaneously. With HPC, it is possible to perform many simulations to generate the three-dimensional structure of  $C_n^2$  from which the two-dimensional structure of  $r_0$  can be characterized. Figure 5 shows an example of a cross section of the  $\log_{10}$  of  $C_n^2$  between Haleakala and Mauna Loa in Hawaii. The effect of surface heat flux from the lava fields on the northern slope of Mauna Loa is clearly seen in the intense  $C_n^2$  indicated by the red colors near the surface. Local features such as land usage and terrain create localized inhomogeneities in surface heat flux and gradients in temperature and wind speed. (Deardorff, 1980). One effect of this is that some areas have better atmospheric seeing on average than other areas. Figure 5 shows the average  $r_0$  (referenced to zenith and 1550 nm) for an area including Maui, HI. The simulations demonstrate the impact of the ocean in suppressing turbulence due to the reduced surface heat fluxes found over water as compared to land (Deardorff, 1980). The results also demonstrate the good seeing at the top of Haleakala near the southern end of Maui. Further analysis indicates certain areas near or just below the peak may have the most favorable conditions, and that wind speed, direction, and localized convergence patterns are major factors in this. WRF simulations can be used in this way to identify localized areas of good atmospheric seeing that could be further investigated with field measurements.

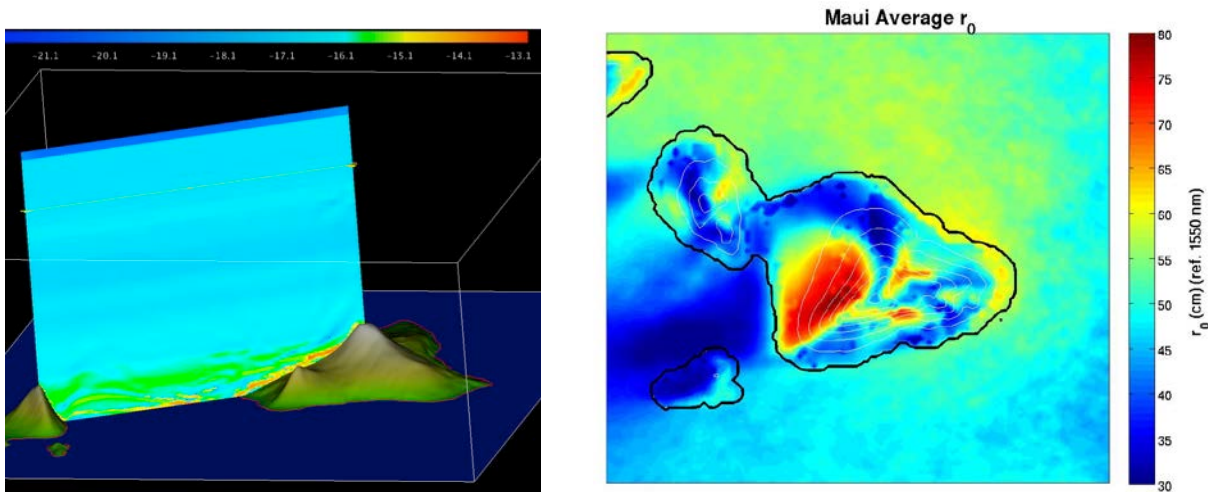


Figure 5 Example of a cross section of  $\log_{10}(C_n^2)$  between Haleakala and Mauna Loa in Hawaii (left) and the average  $r_0$  at 23 UTC (right) simulated by WRF for Maui, HI.

#### 4. SUMMARY AND CONCLUSIONS

Optical turbulence is important to astronomers and designers of free-space optical communications systems because it distorts the optical wavefront, degrading images and causing a reduction in the quality of service of communications links. These scientists and engineers need to know the statistics of the seeing conditions at their locations of interest for site selection, AO system design, and scheduling. Though measurement campaigns have been conducted for a few locations (primarily astronomical observatories), obtaining long-term, validated statistics for most places is impractical and costly.

This investigation into using NWP to characterize optical turbulence has been successful in producing an accurate climatology of optical turbulence. Comparisons of WRF-derived values of  $r_0$  with DIMM measurements demonstrate that WRF is capable of generally describing the climatology of the region of interest. The model does an excellent job simulating the diurnal variation found in  $r_0$ , and differences with observations are generally less than 10%. Although the  $r_0$  statistics shown in this paper are limited to a single grid point in the WRF domain, the simulations can also be used to provide guidance to scientists and engineers for optimizing site location to take advantage of local meteorological, terrain, or land usage features. Though further validation datasets would increase confidence in the simulations, in the absence of such data these WRF simulations can provide a first-order characterization of the optical turbulence for locations of interest.

## 5. ACKNOWLEDGMENTS

The authors thank the Maui High Performance Computing Center (*Mana*) and the Northrop Grumman IS HPC (*Virgo*) center for providing simulation time on their clusters.

## REFERENCES

- Beckers, J., T. Brown, M. Collados, C. Denker, F. Hill, J. Kuhn, M. Penn, H. Socas-Navarro, D. Soltau, and K. Streander, "ATST site survey working group final report," Technical report, National Solar Observatory, <http://atst.nso.edu/> (2004).
- Bougeault, P. and P. Lacarrere, 1989: *Mon. Wea. Rev.*, 117, 3481.
- Deardorff, J. W., "Stratocumulus-capped mixed layers derived from a three-dimensional model," *Bound. Layer Meteorol.*, 18, 495–527 (1980).
- Fried, D. L., "Statistics of a geometric representation of wavefront distortion," *J. Opt.Soc. Amer.*, 55, 1427–1435 (1965).
- Gerrity, J. P., T. L. Black, and R. E. Treadon, "The numerical solution of the Mellor-Yamada level 2.5 turbulent kinetic energy equation in the Eta model," *Mon. Wea. Rev.*, 122, 1640–1646 (1994).
- Kondo, J., O. Kanechika, and N. Yasuda, "Heat and momentum transfers under strong stability in the atmospheric surface layer," *J. Atmos. Sci.*, 35, 1012–1021 (1978).
- Masciadri, E. and P. Jabouille, "Improvements in the optical turbulence parameterization for 3D simulations in a region around a telescope," *Astron. Astrophys.*, 376, 727–734 (2001).
- Mellor, G. L. and T. Yamada, "Development of a turbulence closure model for geophysical fluid problems," *Rev. Geophys. Space Phys.*, 20, 851–875 (1982).
- Skamarock, W. C., J. B. Klemp, J. Dudhia, D. O. Gill, D. M. Barker, M. G. Duda, W. W. X. Y. Huang, and J. G. Powers, "A description of the Advanced Research WRF version 3," Technical report, National Center for Atmospheric Research, [Available on-line at <http://www.mmm.ucar.edu/wrf/users/>] (2008).
- Stull, R., [An Introduction to Boundary Layer Meteorology], Kluwer Academic Publishers, Dordrecht, The Netherlands, 176 pp (1998).
- Tatarski, V. I., "The effects of the turbulent atmosphere on wave propagation," Technical report, U.S. Department of Commerce, NTIS TT-68-50464. 472pp (1971).
- Walters, D. L. and L. W. Bradford, "Measurements of  $r_0$  and  $\theta_0$ : two decades and 18 sites," *Applied Optics*, 36, 7876–7886 (1971).
- Walters, D. L. and D. K. Miller, "Evolution of an upper-tropospheric turbulence event—Comparison of observations to numerical simulations," Preprints, 13th Symposium on Boundary Layer Turbulence, AMS, 157–160, Dallas, TX (1999).